CalDet blessed plots

Mike Kordosky
University College London
(kordosky@hep.ucl.ac.uk)

March 15, 2006

1 Introduction

This document encloses CalDet blessed plots along with captions and some descriptive text. It is intended that the figures be used to support general MINOS talks as introductory material or as backup slides. Several theses[1, 2, 3, 4, 5, 6] and a NIM paper[7] have been written on CalDet and this document borrows liberally from them. The theses, in particular, contain details which this document cannot hope to duplicate.

Note: This document is available in html format at:
http://www.hep.ucl.ac.uk/~kordosky/caldet_blessed/html/caldet_blessed.html
The html version contains links to GIF and EPS versions of each figure as well as figure captions in LaTeX format.

2 Calibration Detector

2.1 Raison d'être

The primary goal of the CalDet is to determine the calorimetric response to electrons, hadrons and muons as a function of particle energy. Furthermore CalDet is used to demonstrate that the Near and Far Detectors can be precisely calibrated relative to each other. In addition to providing the calibration of the MINOS detectors, the CalDet measurements are used to tune the Monte Carlo detector simulation. Moreover, the study of electromagnetic and hadronic event topology provides essential input into the pattern recognition algorithms used to analyze the neutrino data.

2.2 Detector Information

The CalDet steel plates were $1\,\mathrm{m} \times 1\,\mathrm{m}$ square and 2.50 cm-thick. The detector was unmagnetized, in contrast with the magnetized, 2.54 cm-thick planes used in the Near and Far Detectors. The steel was manufactured in the U.K. and has a different composition from the ND and FD steel. The differences are not expected to cause a significant change in the detector response.

The CalDet was composed of five identical sub-sections, with twelve planes in each, allowing relatively easy installation in the test beam areas. The length and type of the readout cables was chosen to mimic the attenuation and therefore light level of the underground detectors. In 2002 one side of each detector plane was read out using 4 m-long ("green") WLS fiber cables while the other side was read out using 6 m-long clear optical fiber cables. This was meant to mimic the FD. In 2003 some data were taken with the detector cabled with 3 m-long green cables connected to PMTs, as well as 1 and 3 m-long green cables terminated with reflector connectors (to simulate the ND attenuation). The attenuation difference between the WLS and clear readout also enables a clean-cut demonstration of the detector calibration.

The CalDet was operated with FD electronics in 2002, ND and FD in 2003, and ND only in 2003. Beam data were mostly collected by triggering the detector on a coincidence of beam counters. Some ND data were taken in sgate mode during 2003. Data were taken with FD electronics and dynode trigger in 2001 but were not very useful as the (asynchronous) dead-time was very high.

3 Calibration

3.1 Brief synopsis of the calibration

The principle tools for calibrating the detector were an LED based light-injection (LI) system, cosmic rays, and test-beam muons. The detector was calibrated in a multi-stage procedure that converted the raw signal $Q_{raw}(i,t)$ measured by channel i at time t into a fully corrected signal Q_{cor}. Each cali-

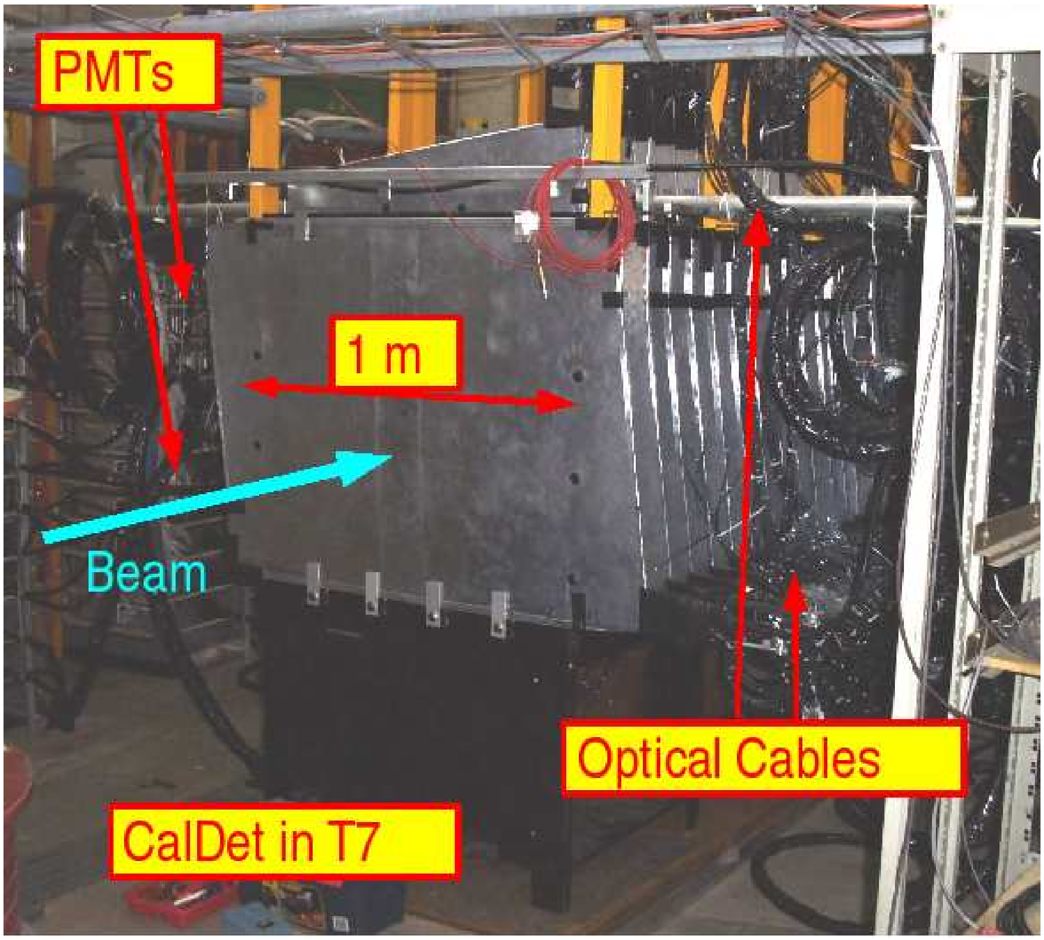

Figure 1: The Calibration detector, located in the CERN PS East Hall T7 beamline. The photo was taken during the 2002 running period.

bration stage produced a numerical factor ("calibration constant"). The fully corrected Q_{cor} was defined as the product of $Q_{raw}(i,t)$ and the calibration constant from each stage:

$$Q_{cor} = Q_{raw}(i,t) \times D(i,t) \times L(i) \times U(i) \times T(t) \times S$$

where D, L, U, T and S refer to:

Drift correction $D(i,t)$: Light injection was used to determine the absolute gain of each channel as well as track the gain over time.

Linearity correction $L(i)$: The LI system was used to linearize the PMT and VA chip response to large signals.

Uniformity correction $U(i)$: Through-going muons were used to account for differences in light output between individual strips and attenuation in the optical fibers.

Temperature correction $T(t)$: The temperature dependent response of the scintillator strips, photomultipliers, and electronics was corrected for.

Signal scale calibration S: The overall scale of the signals was anchored to the detector's response to stopping muons.

4 CalDet Operations

4.1 The PS Test Beams

The CalDet was exposed in the T11 and T7 test beams in the East Experimental Hall of the 24 GeV/c CERN Proton Synchrotron (PS). The beams are dual polarity, mixed composition (e, μ, π and p), and were operated at momentum settings in the range 0.2–3.6 GeV/c (T11) and 1–10 GeV/c (T7). Both lines were equipped with brass collimators for momentum and intensity definition. Two or three scintillator paddles were placed in the beamline and used to measure the particle time of flight (TOF). The two counters were separated by 9.1 m in T7, 12.5 m or 7.3 m in T11, and achieved a resolution of 100–200 ps. Several threshold Čerenkov counters filled with CO_2 were provided to identify electrons at all energies and muons and pions with momenta ≥ 1.8 GeV/c.

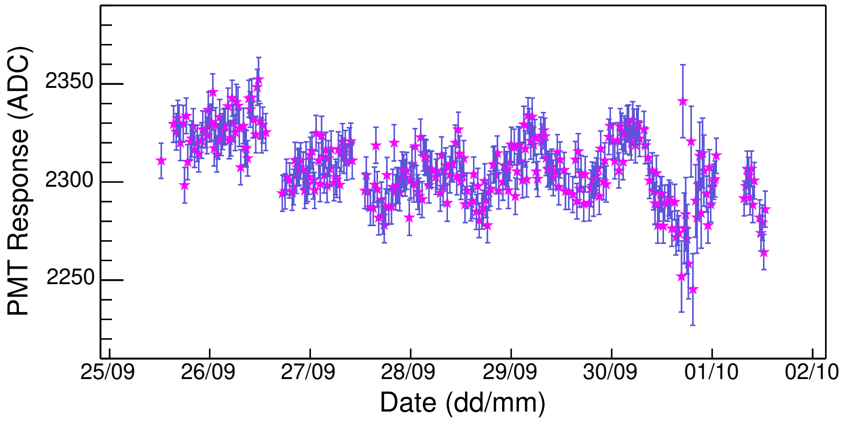

Figure 2: The response of a single PMT channel measured over the course of six days using the light injection system. Each point represents the mean response to 2500 light injection pulses. These data are known as drift points. The oscillatory shape is due to changes in gain with the ambient temperature. The FD electronics was used and the light level was about 35 PE.

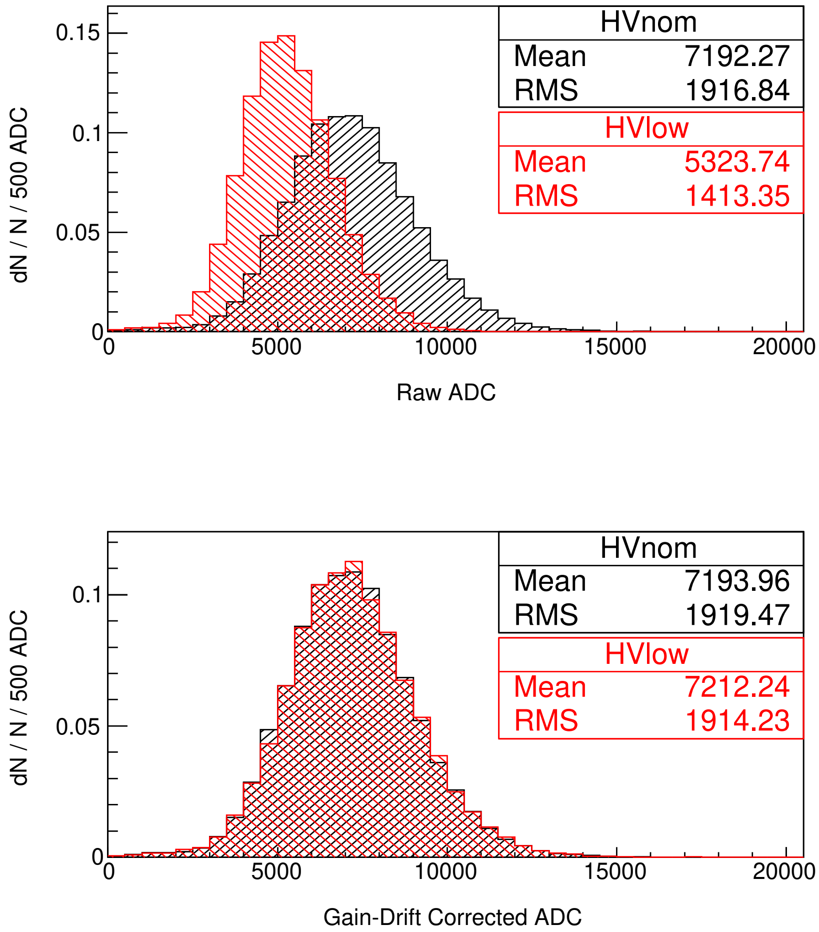

Figure 3: The upper figure shows the summed signal, in uncalibrated ADC counts, measured for 1 GeV/c electrons. Two runs were taken, one with the PMT high voltages at their nominal values and the other after decreasing the high voltage of each PMT by 25 V. The lower figure shows the summed signal after the gain drift correction $(D(i,t))$was applied. The correction was able to reduce a 26% discrepancy to less than 0.5%.

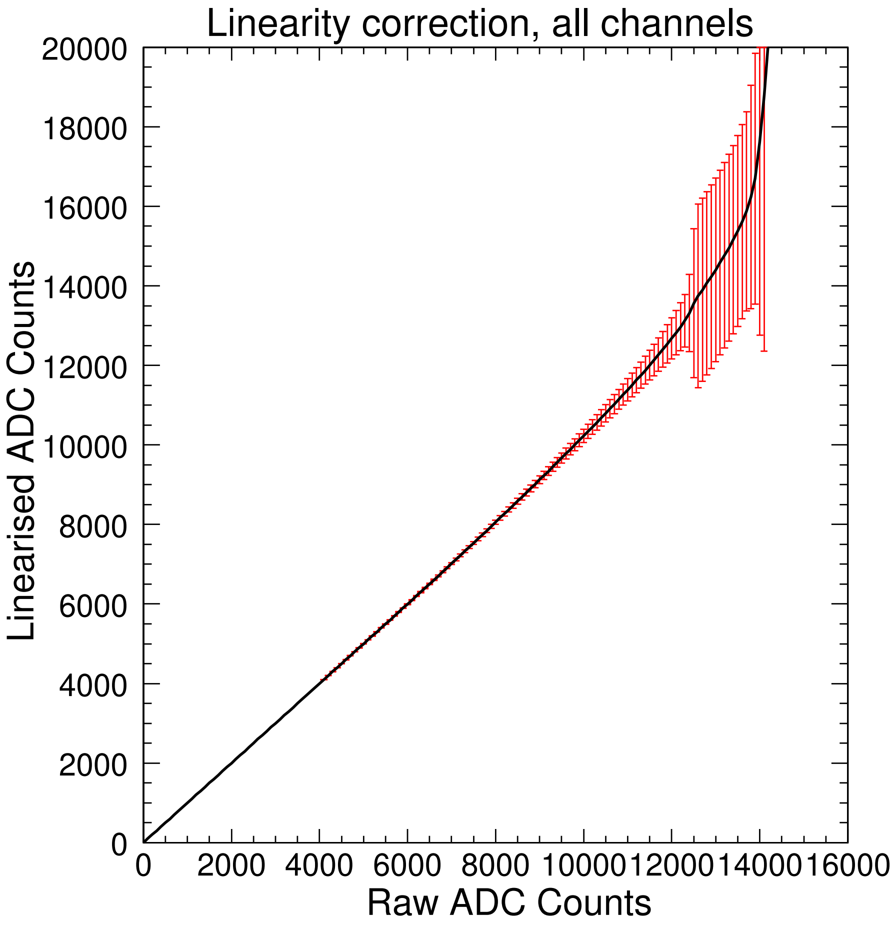

Figure 4: In black, the average linearity correction as a function of Raw ADC counts. The error bars show the RMS (computed over all channels) of the linearity correction. The sharp increase in RMS at approximately 13000 ADC counts occurs as the response of individual channels begins to saturate.

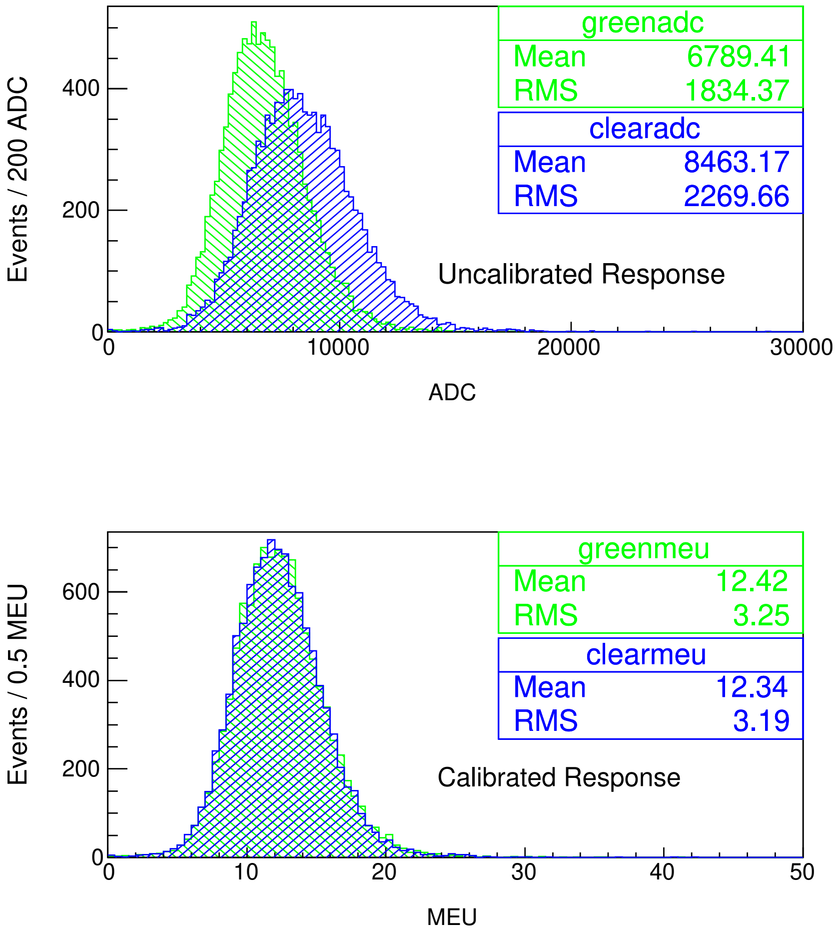

Figure 5: The response of 1 GeV/c electrons when measured through WLS fibers as compared to measured through clear fibers. The top plot shows the response before application of the uniformity calibration constants ($U(i)$) while the bottom shows the calibrated response. Before calibration the response at each end differs by $\sim 20\%$, after calibration, the means agree to better than 1%.

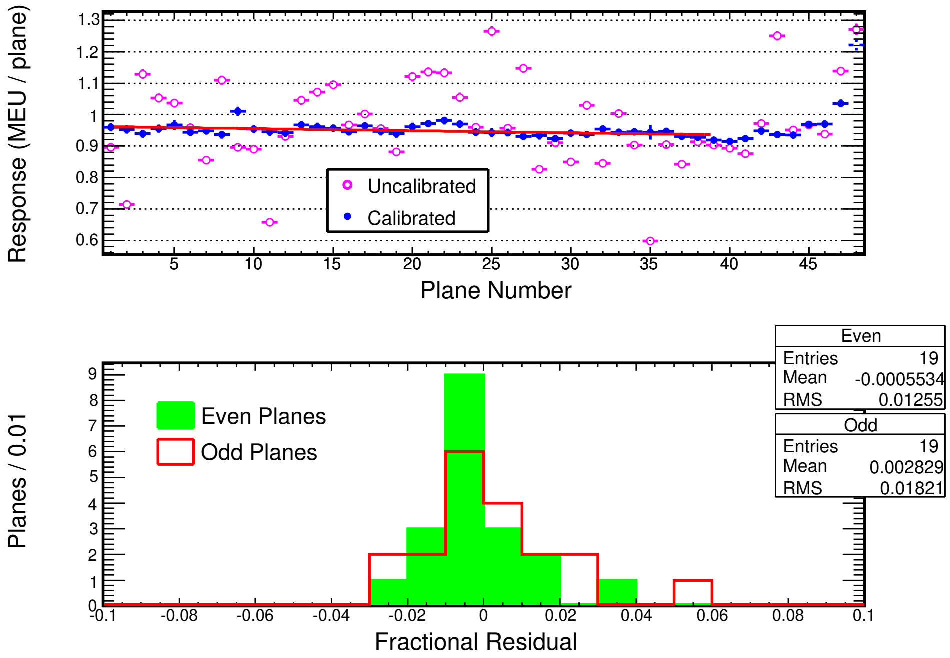

Figure 6: The performance of the strip-to-strip equalization procedure. The upper figure displays the average signal per scintillator plane measured with a sample of 1.8 GeV/c stopping beam muons. The measurements are shown before and after the application of the uniformity calibration ($U(i)$). A linear fit was done to the calibrated points and the residuals were used to fill the histograms in the lower figure. The RMS of the residual distributions indicates the planes were calibrated with an accuracy of $\approx 1.6\%$.

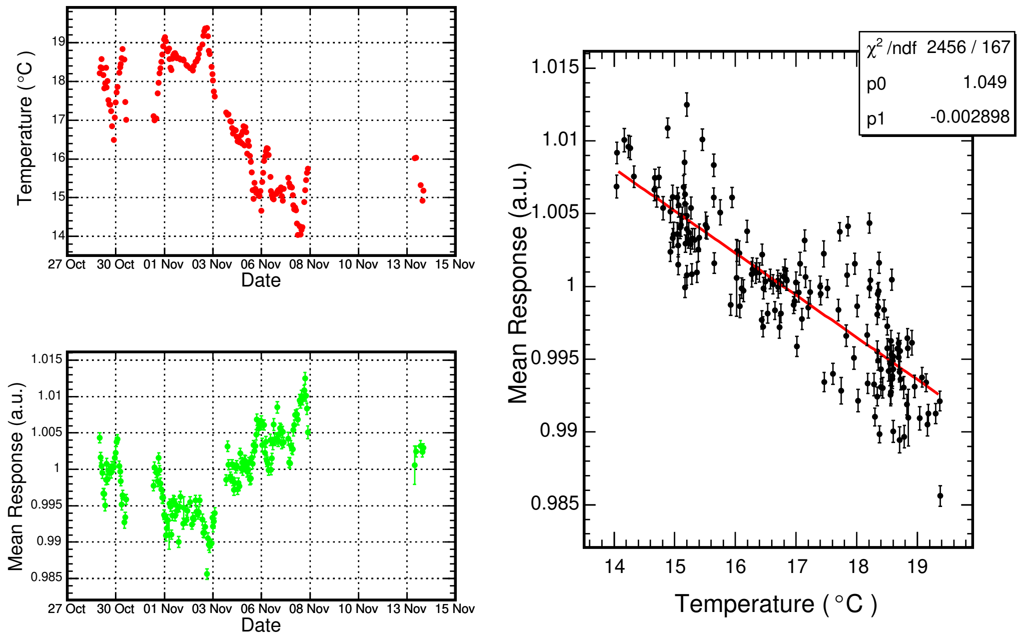

Figure 7: The top left-hand figure shows the average air temperature for each of the runs used in the study. The bottom left-hand figure shows the change in the response (to cosmic ray muons) as a function of time. The right-hand figure shows the response as a function of air temperature, along with a straight line fit used to characterize the dependence.

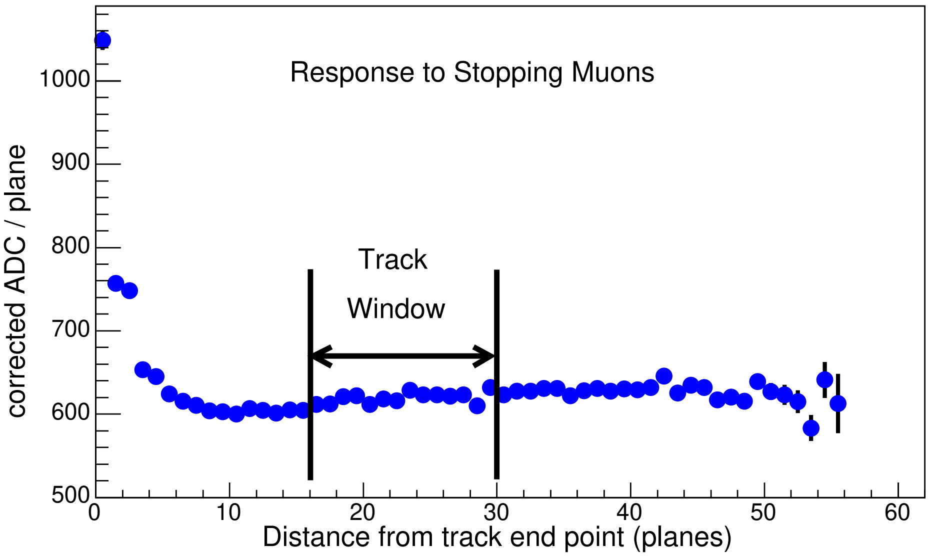

Figure 8: The average response to stopping muons as a function of the distance from the end of the track along with the window used in the signal-scale calibration. The signals were corrected for gain drift, non-linearity, strip light-output non-uniformity and temperature fluctuations.

4.2 External Trigger

The MINOS electronics were designed to operate in the relatively low rate neutrino environment. When operated, without alteration, in the relatively high-rate testbeam environment, the electronics were dominated by dead-time and pile-up effects. To improve performance, a simple trigger was formed from the coincidence of the two time-of-flight counters. The coincidence signal was transmitted to each VARC and used to enable dynode triggers for $\approx 500\,\mathrm{ns}$. A $60\,\mu\mathrm{s}$ veto was then generated to suppress coincidences while the PMT signals were being digitized. The typical coincidence rate was $1\,\mathrm{kHz}$, a result of balancing the data rate against the effect of pile-up. An additional facility was included in the trigger logic to allow light-injection and cosmic ray calibration events to be collected between beam extractions.

4.3 Offline Event Finding

The data acquisition continuously appended newly recorded hits to the set of previously observed hits, flushing the entire record to disk once each second. While collecting beam data, no manipulation (aside from sorting the hits in time order) or online selection was done, so that the data would be as free from bias as possible. The raw data file was processed offline with an algorithm that located events in the stream of hits and then wrote each event as an individual record in a second file. The algorithm began by searching for clusters of hits separated by time gaps of more than $\sim 156\,\mathrm{ns}$. Each group of hits was then tested for the following trigger conditions:

1. proximity (within 156 ns) to a coincidence between the beam counters
2. proximity to a signal from the Čerenkov counters
3. hits in N out of N+1 consecutive scintillator planes, with N=3,4,5
4. proximity to a light injection calibration pulse

Hit clusters that satisfied one of these criteria were flagged with an appropriate trigger word and written to disk. Generally, the first two criteria denoted beam events, while cosmic rays and out-of-spill, accelerator-produced muons were identified with the third criterion. The gap searching algorithm described above is quite similar to the one used by the FD DAQ.

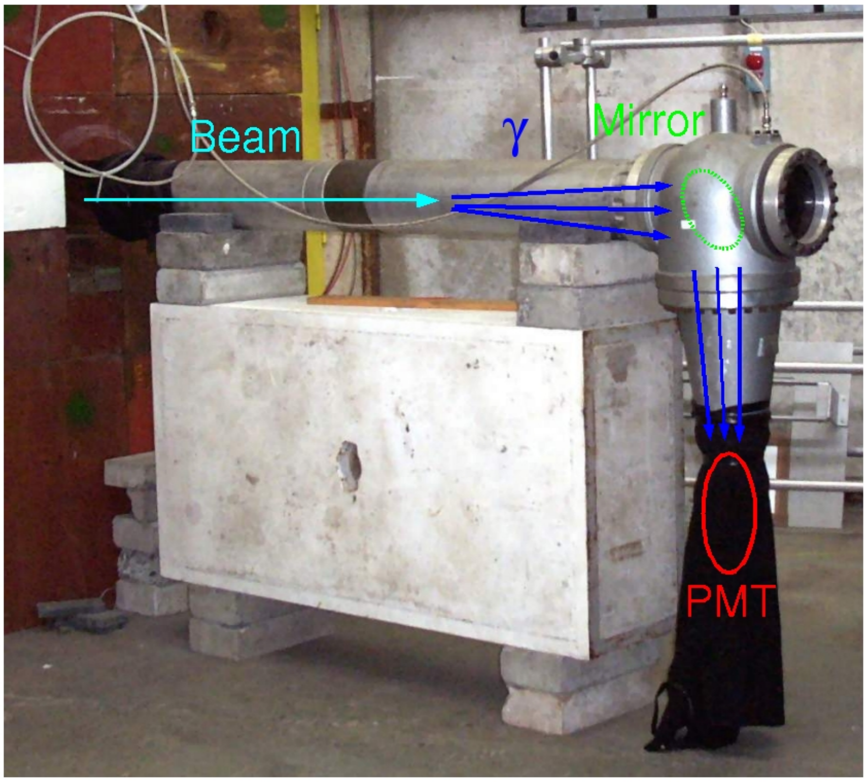

Figure 9: A threshold Čerenkov counter used in the T7 beamline. The counter was filled with carbon-dioxide and at the maximum pressure (4.4 atm) could discriminate between 1.8 GeV/c muons and pions. The electron identification was better than 99% at a typical (for few-GeV beam momentum) pressure of 1 atm.

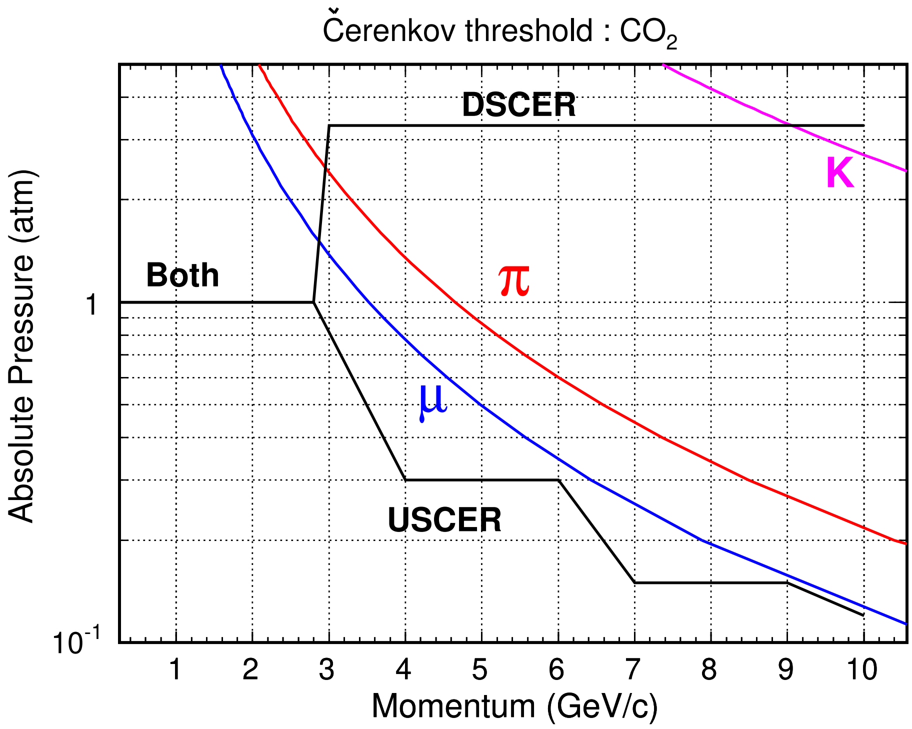

Figure 10: Figure shows the pressure used in the Čerenkov counters as a function of the beam momentum. Various special runs were taken with different pressures, but the values shown here are typical. Two counters were used in T7. Below 3 GeV/c both counters were used to tag electrons. Above 3 GeV/c the downstream (DS) counter was used to tag pions and the upstream counter was operated so as to only identify electrons. The single counter in T11 was operated at approximately 1 atm and was only used to identify electrons.

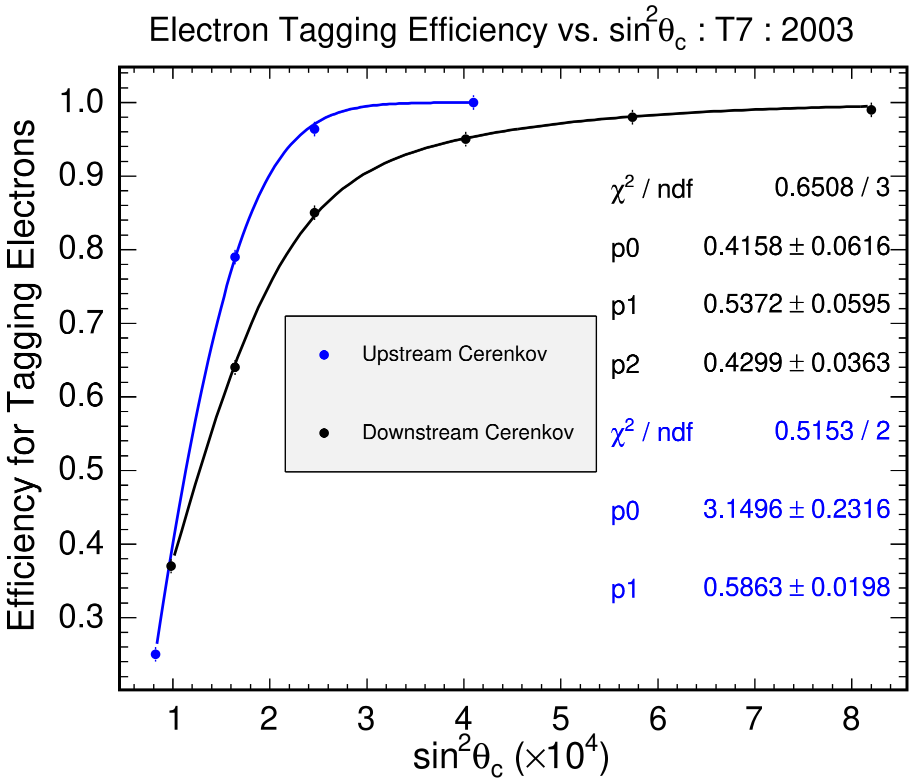

Figure 11: The electron identification efficiency as a function of $\sin^2(\theta_c) \approx 2k\rho - m^2/p^2$ where ρ is the pressure, k is a gas constant, and m, p are the particle's mass and momentum. The data were derived in T7 by pressurising one of the two counters to 4 atm and then measuring the fraction of events triggering the other counter as a function of the gas pressure. Beam counters (scintillator paddles) were used to assure that the particle trajectory passed through both Čerenkov counters.

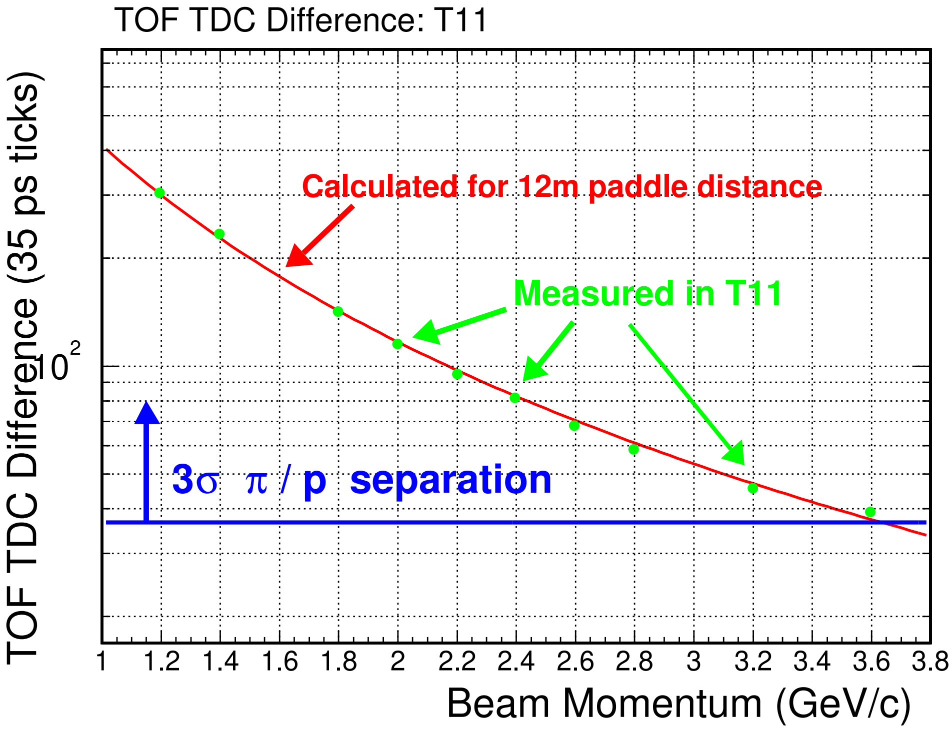

Figure 12: Proton/pion discrimination via time-of-flight as a function of momentum setting. The time-of-flight was used to discrimanate below 4 GeV and Čerenkov above 4 GeV. Two paddles, seperated by 7,9 12 m were used in 2002 . In 2003 a second set of paddles was employed so as to require a coincidence at both ends of the baseline. The paddles were read out by Philips XP2030 or XP2230 photomultipliers. Digitisation was done with a CAEN 775 TDC (35 ps LSB)

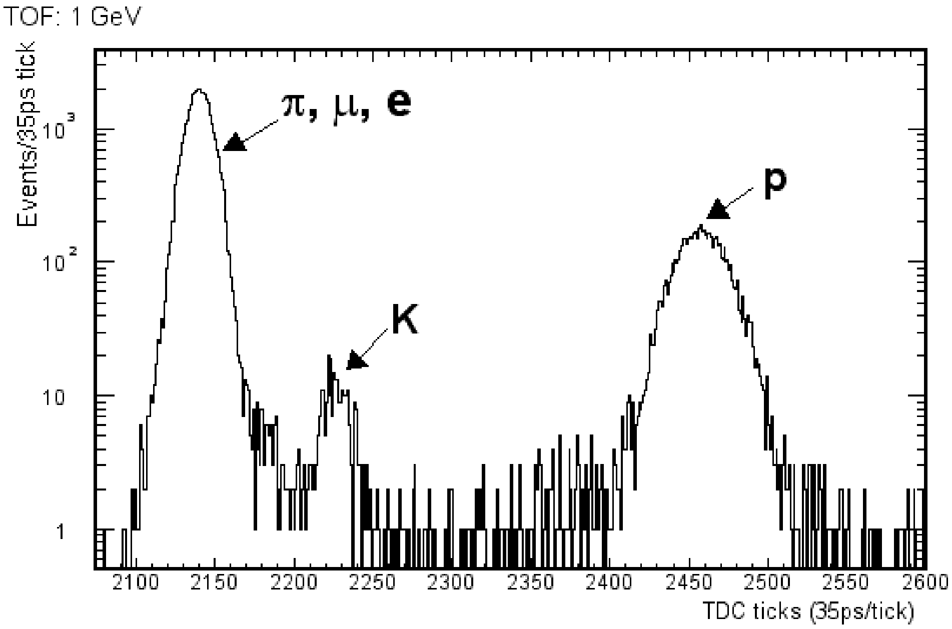

Figure 13: The time-of-flight distribution measured in T11 at 1 GeV/c (positive beam polarity).

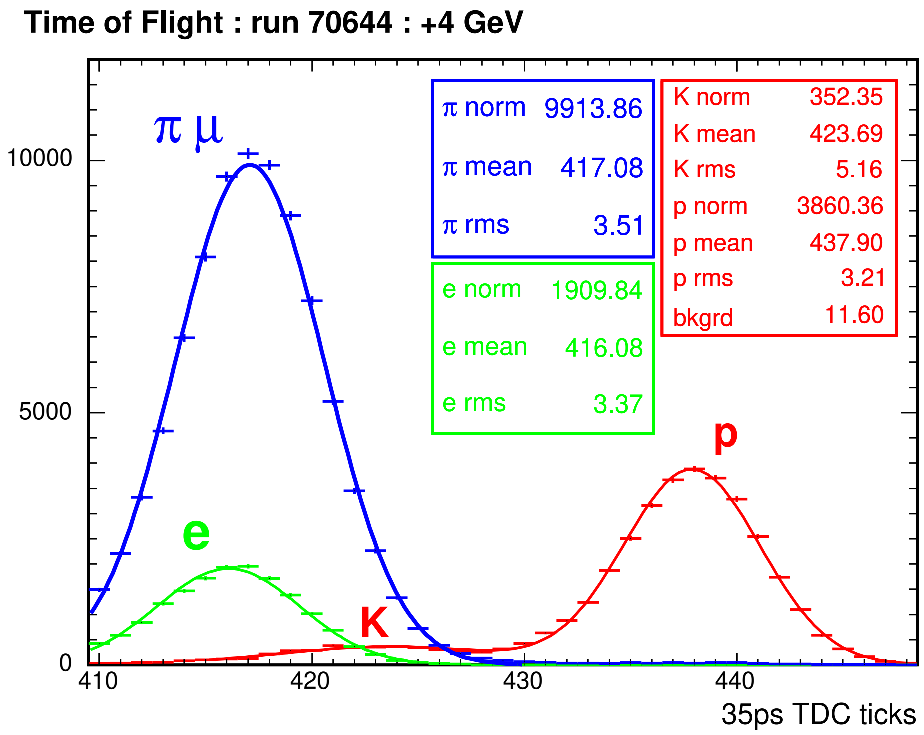

Figure 14: The time-of-flight distribution measured in T7 at 4 GeV/c. One Čerenkov counter was pressurised to identify e, π, μ, yielding the blue distribution. The other Čerenkov counter was pressurised to identify e only. The green distribution are those data collected when both Čerenkov counters triggered. The red distribution are those data collected when neither Čerenkov couter triggered and corresponds to K, p. The time-of-flight and Čerenkov identification are in good agreement and the time-of-flight resolution is 112-125 ps

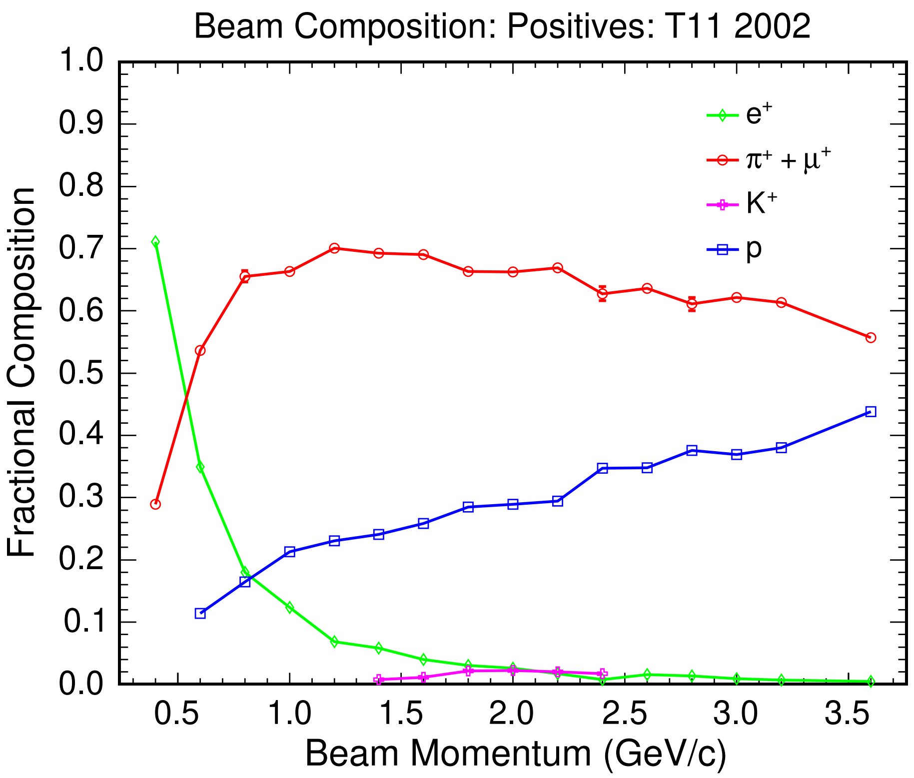

Figure 15: The composition of the T11 beamline (positive polarity) as measured by the Čerenkov and time-of-flight detectors.

5 Results

5.1 Beam Composition

5.2 Response

5.3 Resolution

5.4 Hadron Topology

References

[1] C. Smith, Calibration of the MINOS Detectors and Extraction of Neutrino Oscillation Parameters, Ph.D. thesis, University College London

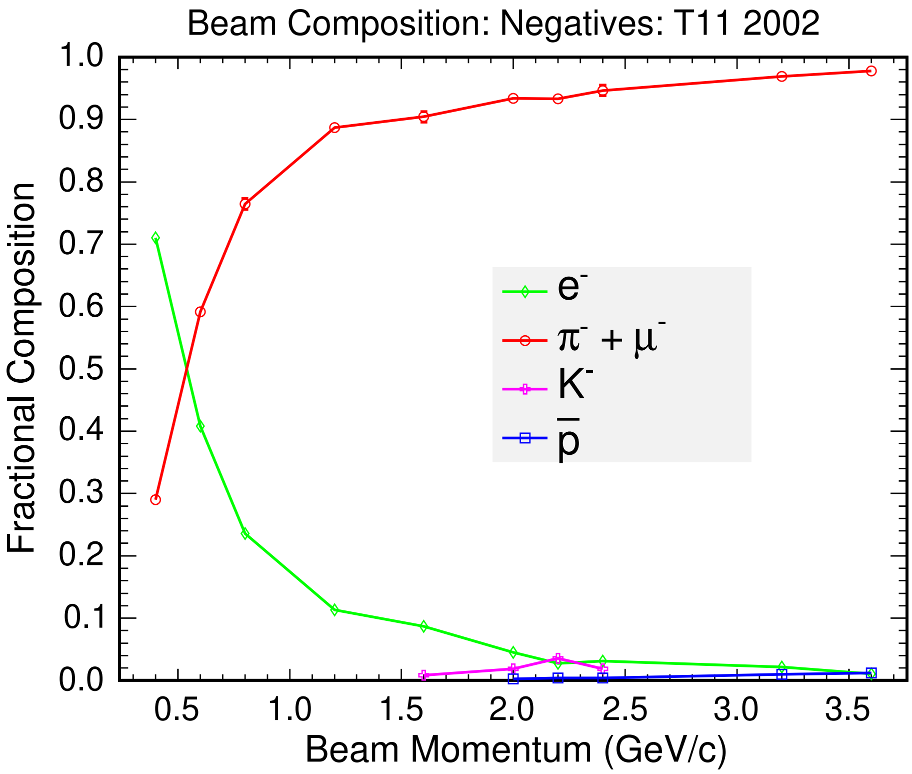

Figure 16: The composition of the T11 beamline (negative polarity) as measured by the Čerenkov and time-of-flight detectors.

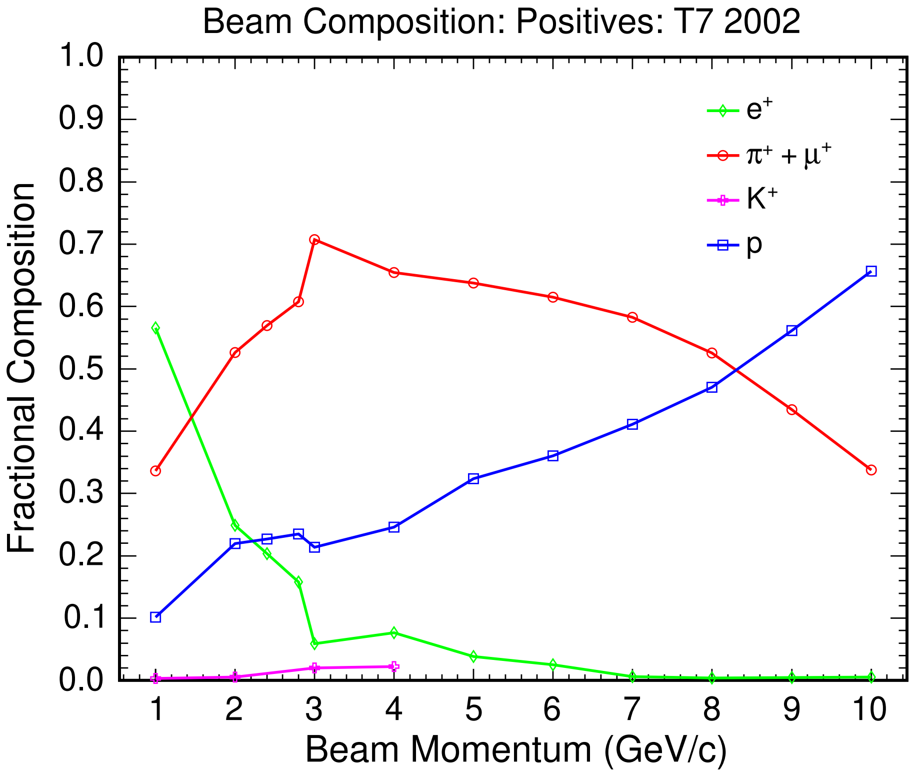

Figure 17: The composition of the T7 beamline (positive polarity) as measured by the Čerenkov and time-of-flight detectors.

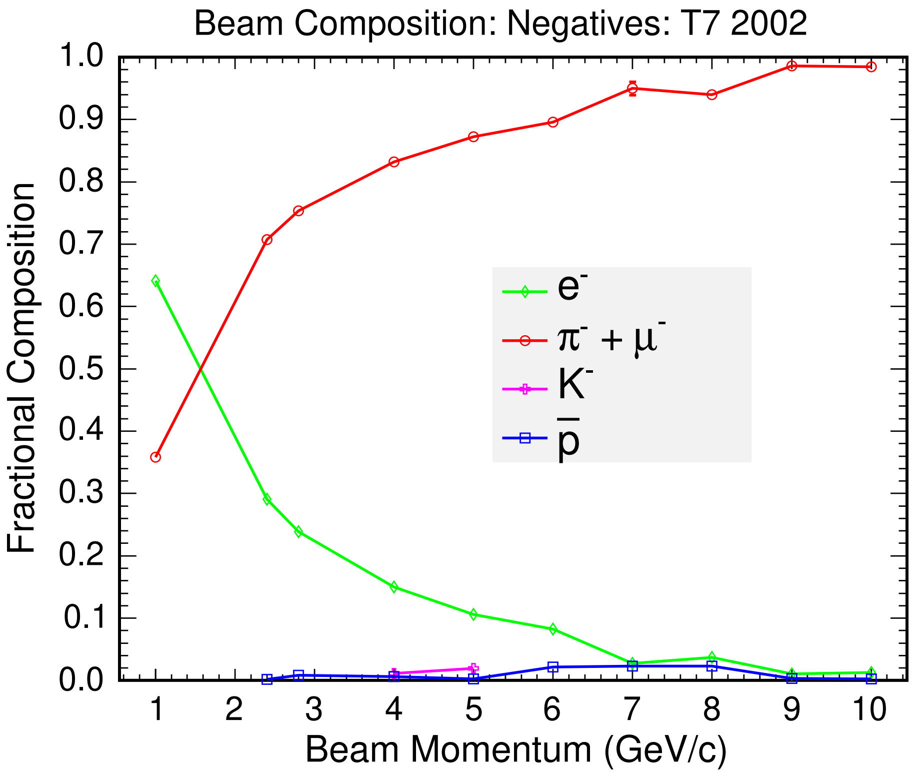

Figure 18: The composition of the T7 beamline (negative polarity) as measured by the Čerenkov and time-of-flight detectors.

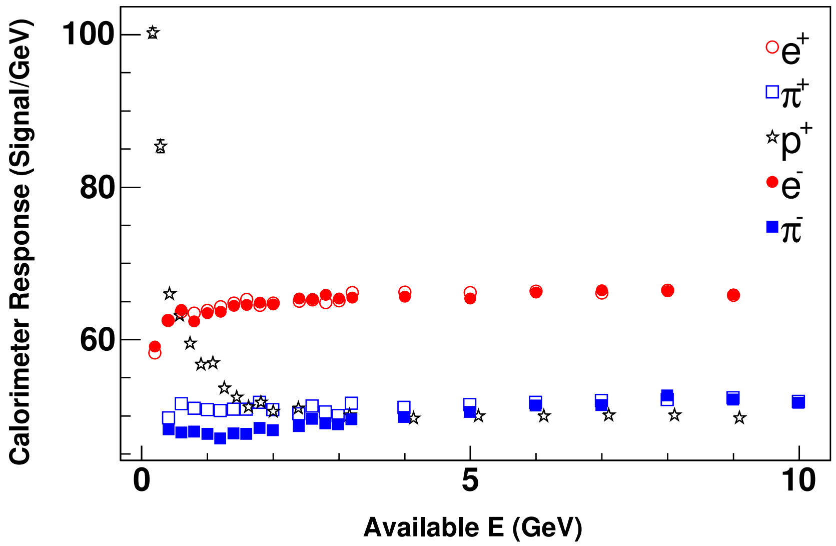

Figure 19: The measured detector response to electrons and hadrons of both polarities. The response is defined as the average summed signal divided by the available energy (total for mesons, kinetic for baryons and electrons). The signal is expressed in historical units ("CalDet MIPs") which correspond to $\approx 2.6\,\mathrm{MEU}$. Error bars are generally to small to be seen but account for the statistical error in the mean (gaussian approximation) as well as the more dominant ($\approx 1\%$) uncertainty in the beam momentum derived from the variation in the electron response for repeated measurements at the same momentum setting. For reference, at 1 GeV the response was $\pi^+ \approx 19.5\,\mathrm{MEU/GeV}$, $\pi^- \approx 18.3\,\mathrm{MEU/GeV}$, $e^\pm \approx 24.8\,\mathrm{MEU/GeV}$, $p \approx 21.0\,\mathrm{MEU/GeV}$.

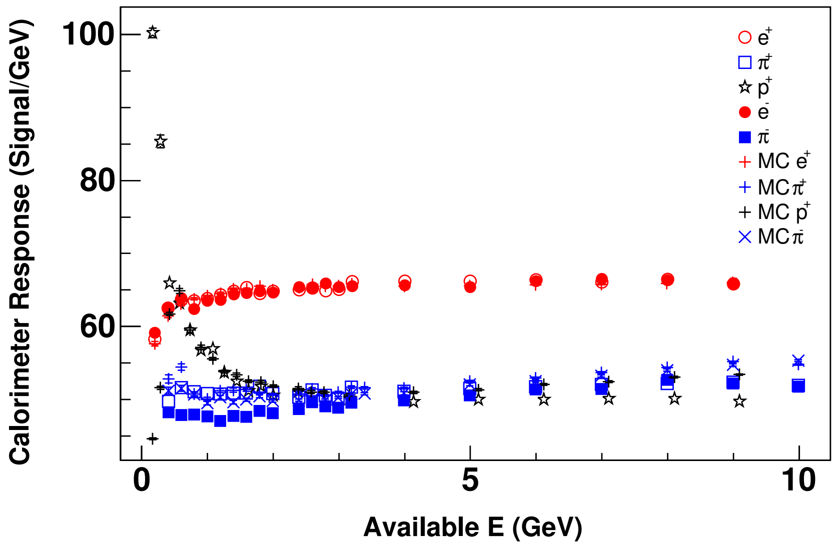

Figure 20: The measured detector response to electrons and hadrons of both polarities compared with the GEANT3 simulation of CalDet. The response is defined as the average summed signal divided by the available energy (total for mesons, kinetic for baryons and electrons). The signal is expressed in historical units ("CalDet MIPs") which correspond to $\approx$ 2.6 MEU. Error bars are generally to small to be seen but account for the statistical error in the mean (gaussian approximation) as well as the more dominant ($\approx$ 1%) uncertainty in the beam momentum derived from the variation in the electron response for repeated measurements at the same momentum setting. For reference, at 1 GeV the response was $\pi^+ \approx 19.5\,\mathrm{MEU/GeV}$, $\pi^- \approx 18.3\,\mathrm{MEU/GeV}$, $e^\pm \approx 24.8\,\mathrm{MEU/GeV}$, $p \approx 21.0\,\mathrm{MEU/GeV}$.

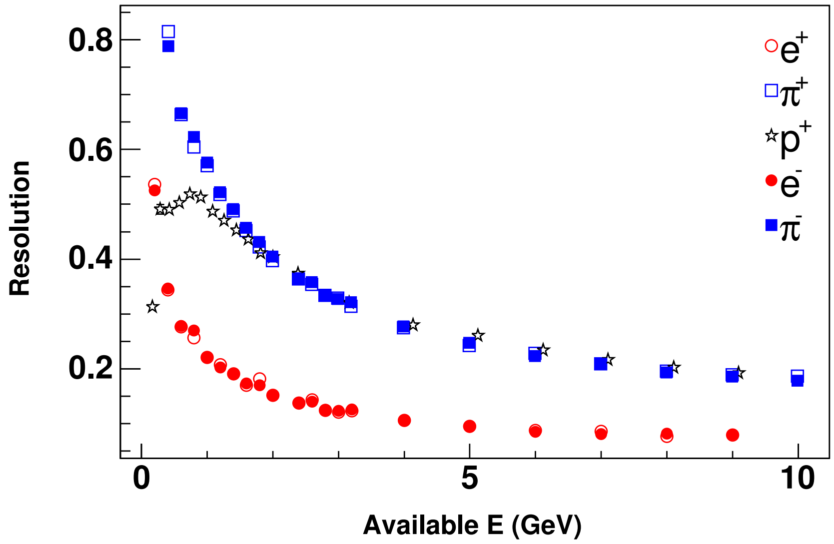

Figure 21: The measured resolution for electrons and hadrons of both polarities. The resolution is defined as the RMS of the summed signal distribution divided by the mean. The response may be parameterised as: $\pi^{\pm} = (2.1 \pm 1.5) \oplus \frac{56.1 \pm 0.3}{\sqrt{E}}$, $p = (4.2 \pm 1.4) \oplus \frac{56.6 \pm 0.6}{\sqrt{E}}$ and $e^{\pm} = (4.1 \pm 1.4) \oplus \frac{24.1 \pm 0.1}{\sqrt{E}}$. For protons the fits were restricted to the region above 1.5 GeV where most protons shower before ranging out.

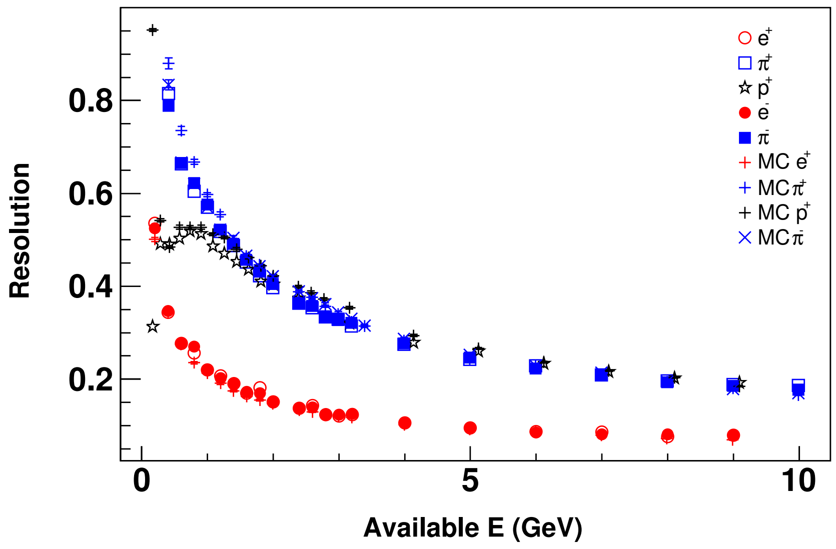

Figure 22: The measured resolution for electrons and hadrons of both polarities compared to the GEANT3 simulation of CalDet. The resolution is defined as the RMS of the summed signal distribution divided by the mean. The response may be parameterised as: $\pi^{\pm} = (2.1 \pm 1.5) \oplus \frac{56.1\pm0.3}{\sqrt{E}}$, $p = (4.2 \pm 1.4) \oplus \frac{56.6\pm0.6}{\sqrt{E}}$ and $e^{\pm} = (4.1 \pm 1.4) \oplus \frac{24.1\pm0.1}{\sqrt{E}}$. For protons the fits were restricted to the region above 1.5 GeV where most protons shower before ranging out.

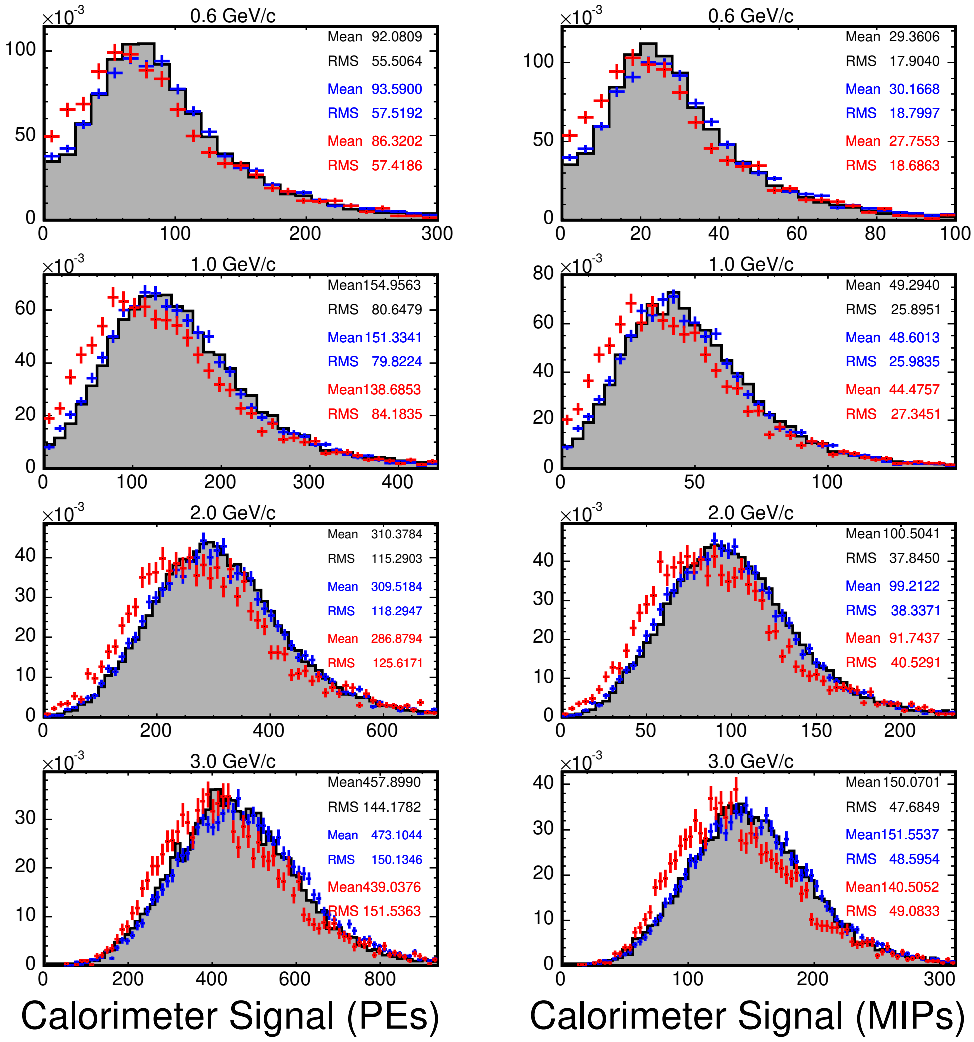

Figure 23: Signal distrubitions ("line shapes") for π^+. The shaded histogram shows the data, blue (red) crosses denote the GCALOR (SLAC-GEISHA) shower simulation.

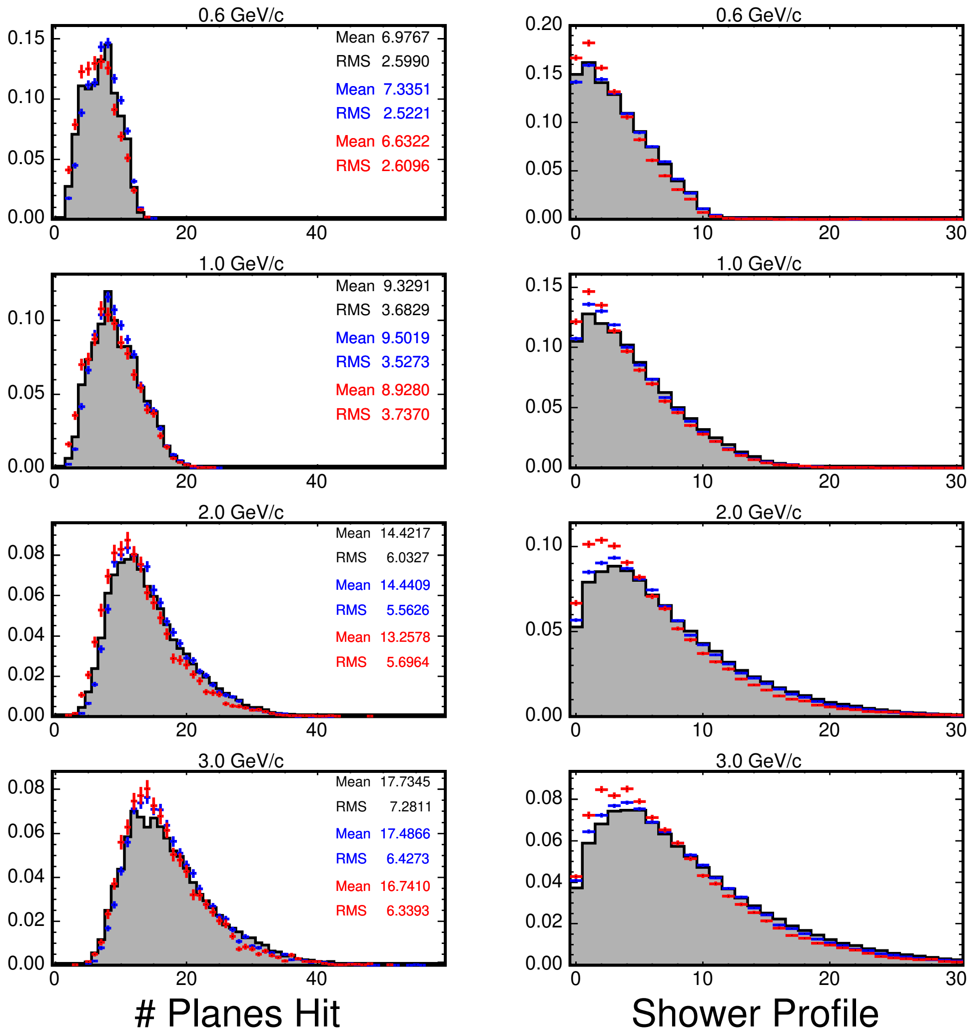

Figure 24: The distribution of the number of planes with a hit (left column) and shower profile (right column) for π^+. The shower profile is defined as the average fraction of the total signal deposited in each plane expressed as a function of the plane number starting at the front of the CalDet. Error bars denote the error on the mean rather than the RMS. The shaded histogram shows the data, blue (red) crosses denote the GCALOR (SLAC-GEISHA) shower simulation.

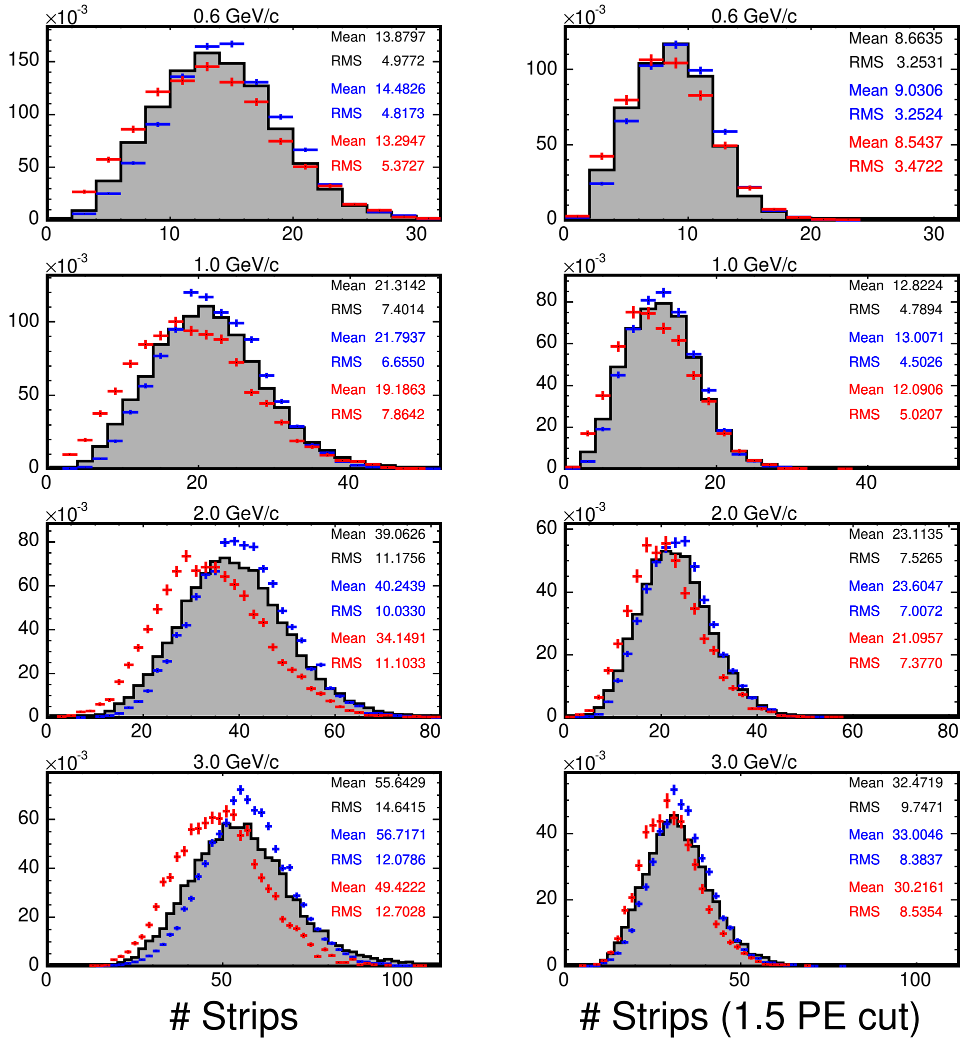

Figure 25: Distributions, for π^+, of the number of hits strips before (left column) and after a 1.5 PE pulseheight cut. The shaded histogram shows the data, blue (red) crosses denote the GCALOR (SLAC-GEISHA) shower simulation.

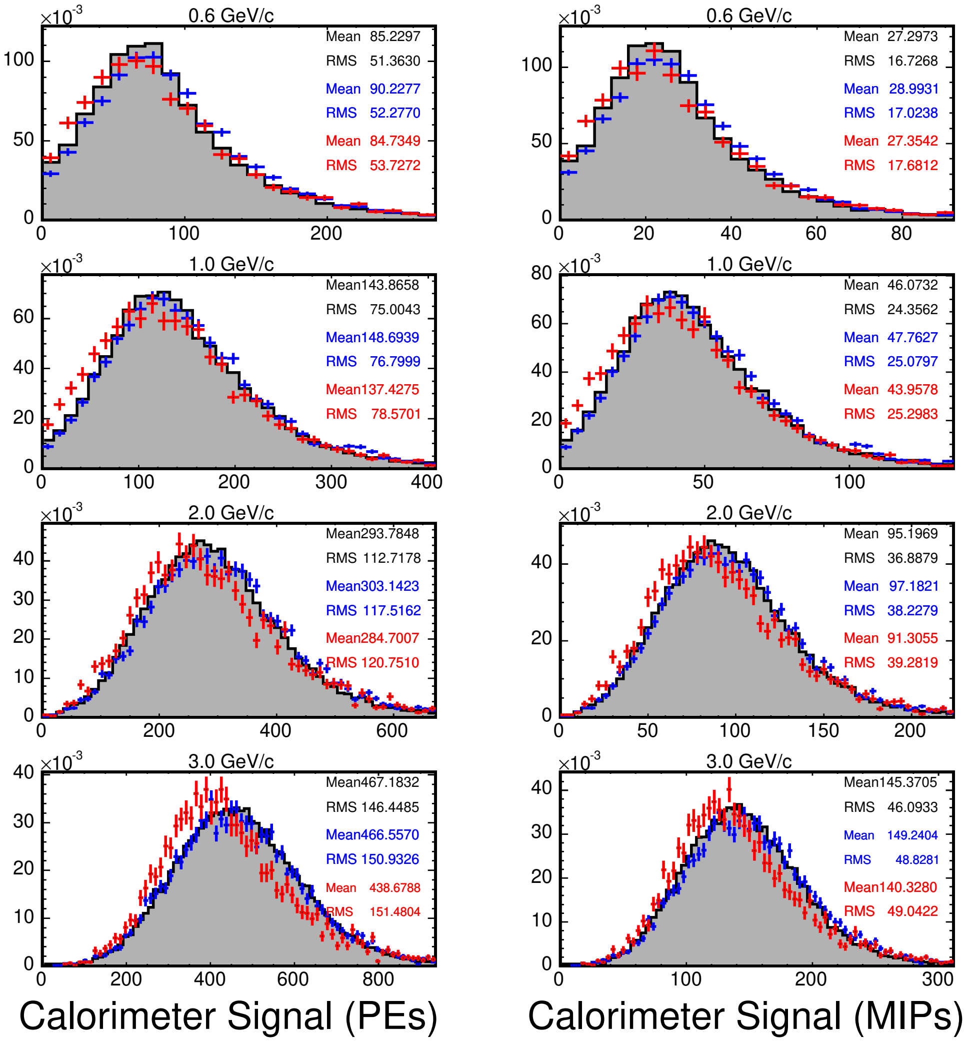

Figure 26: Signal distrubitions ("line shapes") for π^-. The shaded histogram shows the data, blue (red) crosses denote the GCALOR (SLAC-GEISHA) shower simulation.

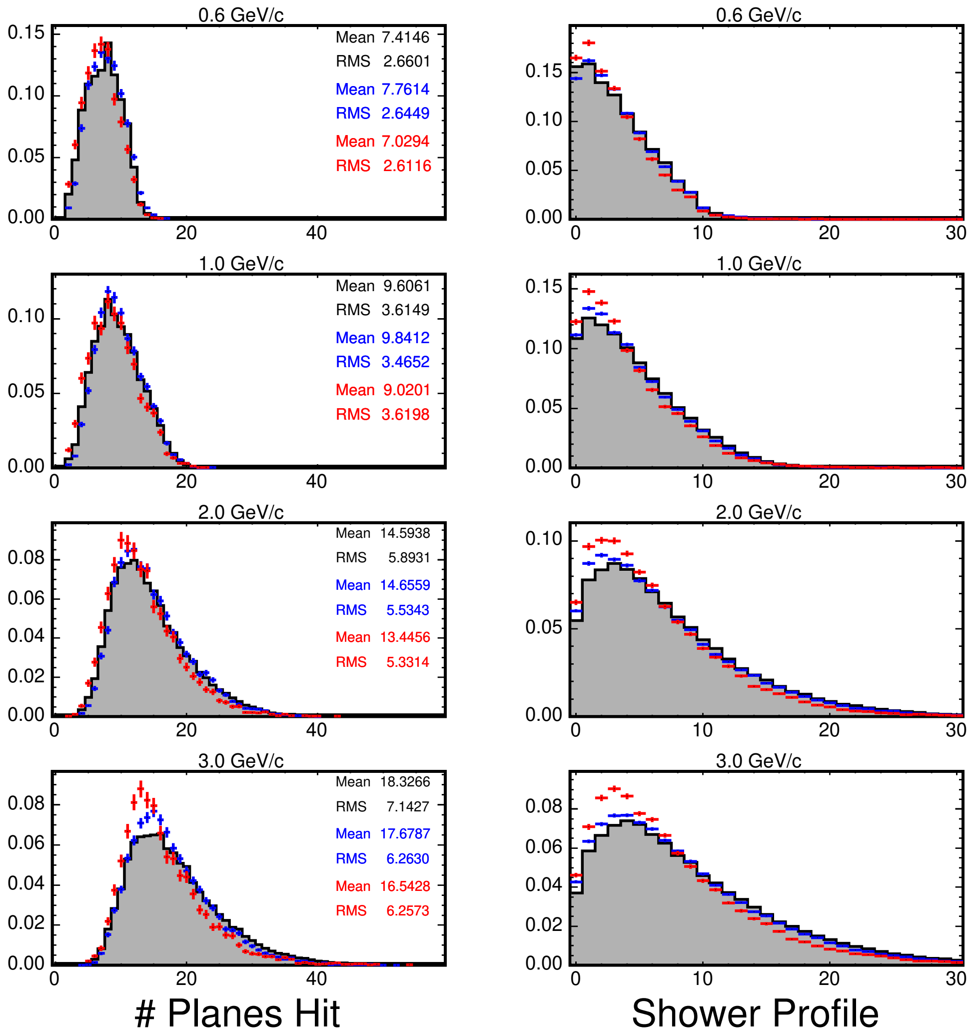

Figure 27: The distribution of the number of planes with a hit (left column) and shower profile (right column) for π^-. The shower profile is defined as the average fraction of the total signal deposited in each plane expressed as a function of the plane number starting at the front of the CalDet. Error bars denote the error on the mean rather than the RMS. The shaded histogram shows the data, blue (red) crosses denote the GCALOR (SLAC-GEISHA) shower simulation.

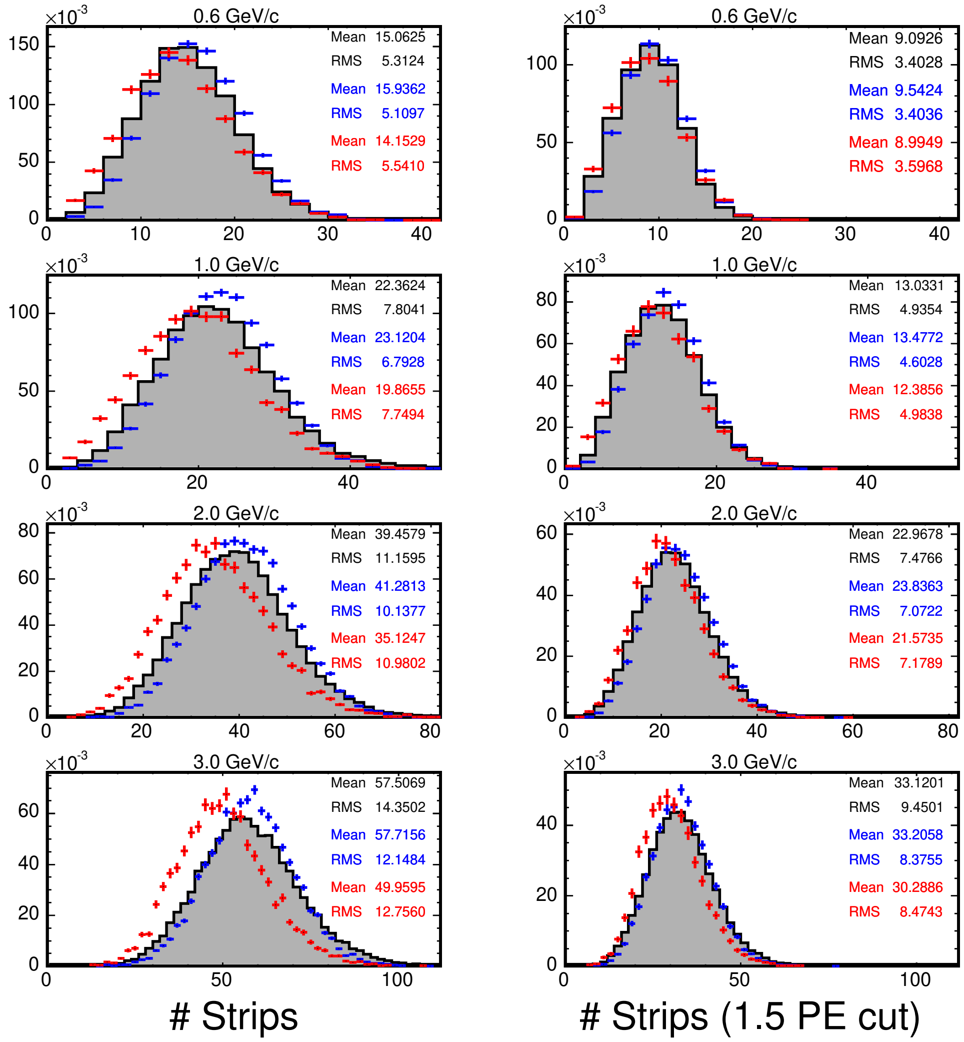

Figure 28: Distributions, for π^-, of the number of hits strips before (left column) and after a 1.5 PE pulseheight cut. The shaded histogram shows the data, blue (red) crosses denote the GCALOR (SLAC-GEISHA) shower simulation.

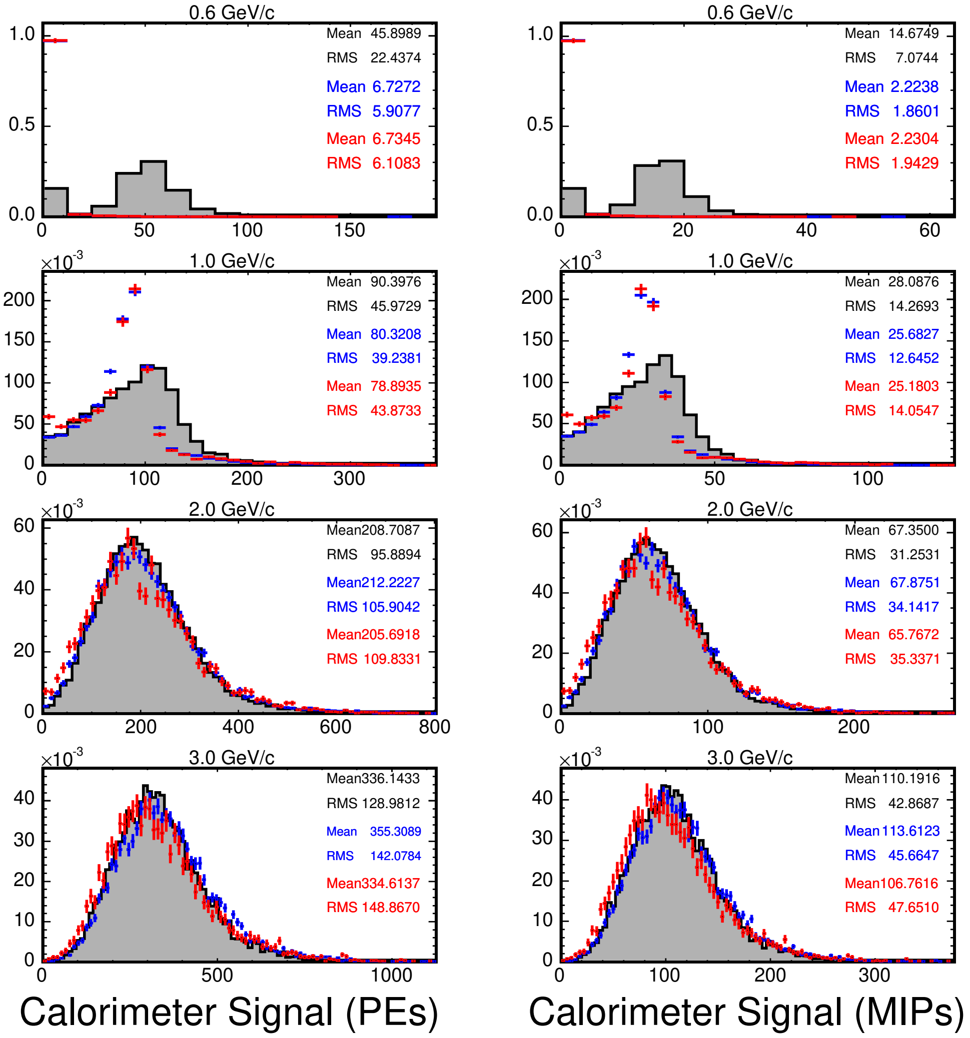

Figure 29: Signal distrubitions ("line shapes") for protons. The shaded histogram shows the data, blue (red) crosses denote the GCALOR (SLAC-GEISHA) shower simulation. Caution: 600 MeV protons barely make it through one plane simply based on ionisation. Losses upstream of CalDet are large for these particles and are somewhat difficult to simulate. Few % differences in the MC proton energy can do much to rectify the (apparently) dramatic differences in the upper figures.

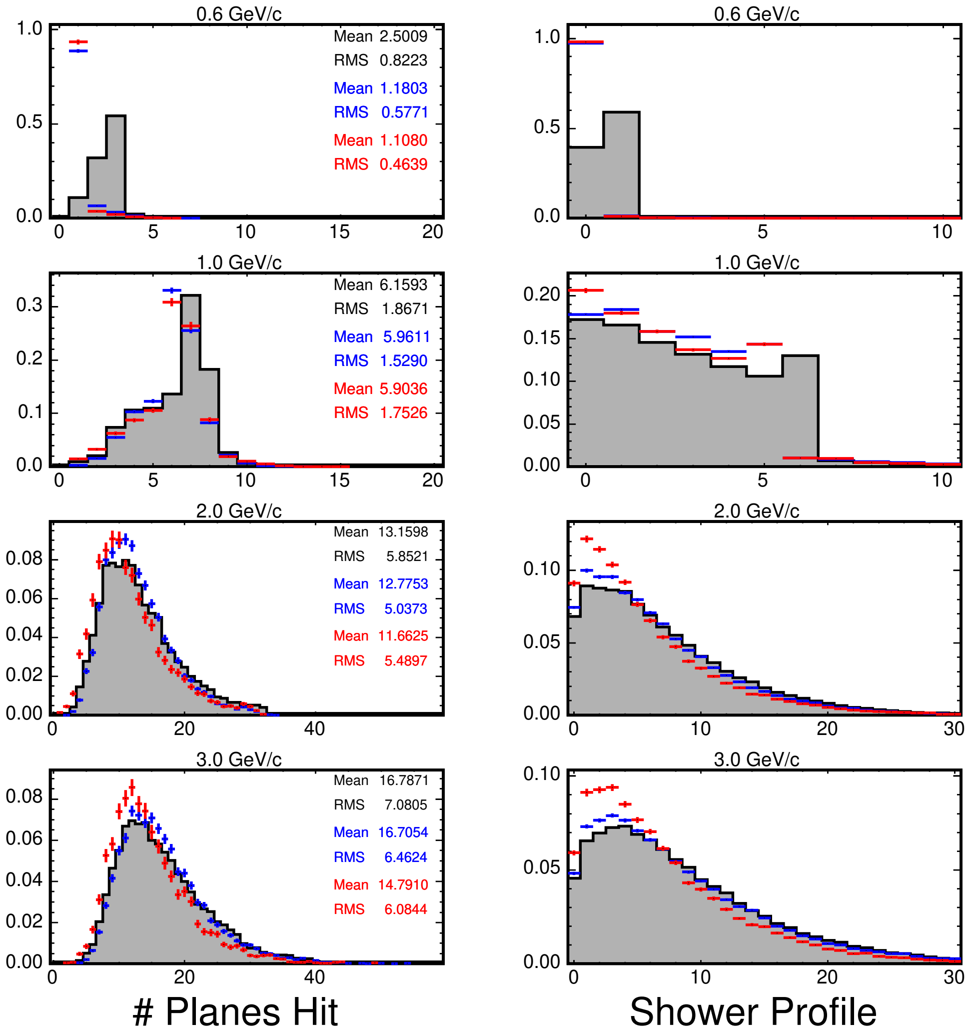

Figure 30: The distribution of the number of planes with a hit (left column) and shower profile (right column) for protons. The shower profile is defined as the average fraction of the total signal deposited in each plane expressed as a function of the plane number starting at the front of the CalDet. Error bars denote the error on the mean rather than the RMS. The shaded histogram shows the data, blue (red) crosses denote the GCALOR (SLAC-GEISHA) shower simulation. Few % differences in the MC proton energy can do much to rectify the (apparently) dramatic differences in the upper figures

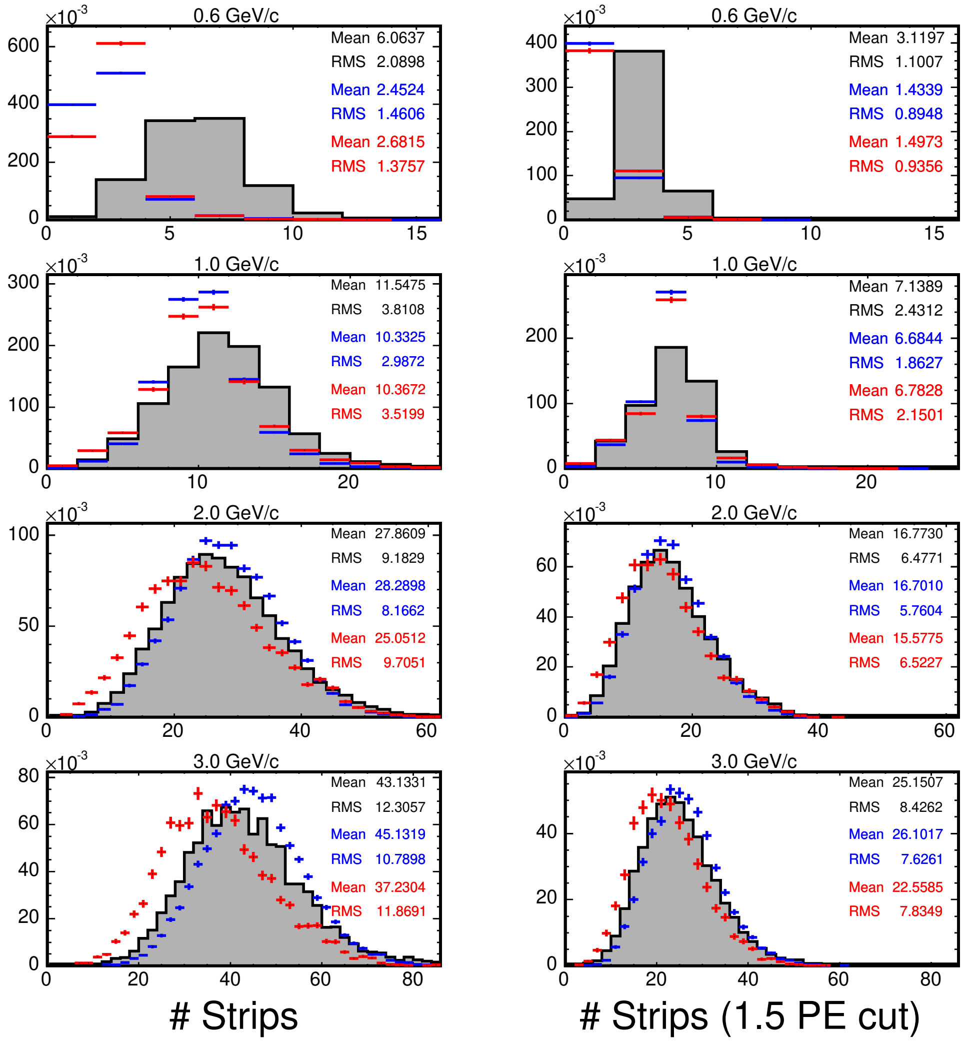

Figure 31: Distributions, for protons, of the number of hits strips before (left column) and after a 1.5 PE pulseheight cut. The shaded histogram shows the data, blue (red) crosses denote the GCALOR (SLAC-GEISHA) shower simulation. Few % differences in the MC proton energy can do much to rectify the (apparently) dramatic differences in the upper figures

(2002).

[2] R. Nichol, Calibration of the MINOS Detectors, Ph.D. thesis, University College London (2003).

[3] M. A. Kordosky, Hadronic Interactions in the MINOS Detectors, Ph.D. thesis, University of Texas (2004).

[4] P. L. Vahle, Electromagnetic Interactions in the MINOS Detectors, Ph.D. thesis, University of Texas (2004).

[5] A. Cabrera, Systematic Comparison of the MINOS Near and Far Detector Readout Systems, Ph.D. thesis, Oxford University (2004).

[6] J. J. Hartnell, Measurement of the MINOS Detectors' Relative Calorimetric Energy Response, Ph.D. thesis, St. John's College, Oxford (2005).

[7] P. Adamson, et al., The MINOS Calibration Detector, Nucl. Instrum. Meth. A556 (2006) 119–133.